Available online at www.sciencedirect.com
SCIENCE DIRECT®
International Journal of Heat and Mass Transfer 47 (2004) 2097–2108
International Journal of HEAT and MASS TRANSFER
www.elsevier.com/locate/ijhmt

Heat transfer enhancement of impinging jets using mesh screens

D.W. Zhou, Sang-Joon Lee *

Department of Mechanical Engineering, Pohang University of Science and Technology, San 31, Hyoja-dong, Pohang 790-784, South Korea

Received 10 May 2003; received in revised form 11 December 2003

Abstract

The heat transfer characteristics of a sharp-edged orifice jet impinging on a flat plate were investigated experimentally with varying the solidity of the mesh screen (σ_s) installed in front of the jet nozzle. The screen modified the flow structure of the free jet, leading to a change in the local heat transfer characteristics. For nozzle-to-plate spacings of $z/d \leqslant 4$, the turbulence intensity was increased with mesh solidity, causing an increase in the local heat transfer rate. For the screen of $\sigma_s = 0.83$, the local maximum heat transfer rate was increased about 3.92% at $z/d = 4$ and the average Nusselt numbers was enhanced about 1.38% at $z/d = 2$, compared with those for the case of no screen.

Keywords: Jet impingement; Heat transfer; Solidity ratio; Flow visualization

1. Introduction

Impinging jets have been extensively utilized to enhance the heat transfer rate in heating and cooling systems. Industrial applications of impinging jets include the tempering of glasses, the drying of papers and textiles, and the cooling of metal sheets, turbine blades and electronic components. Numerous experimental and numerical investigations have been carried out to elucidate the characteristics of jet impingement-induced heat transfer.

Recently, various flow control techniques have been employed to further enhance the impingement heat transfer rate. Some examples are modification of the nozzle configuration [1,2], acoustic excitation, adoption of a perforated plate, and use of a swirling jet. Lee and Lee [2] compared the stagnation heat transfer rate for various nozzle exit configurations and found that varying the nozzle configuration is a simple and effective way to enhance heat transfer. Guo et al. [3] found that the convective heat transfer was enhanced by decreasing the intersection angle between the velocity and temperature gradients. All the above flow control techniques enhance the convective heat transfer rate by modifying the flow structure of the impinging jet. The heat transfer coefficient on the impingement plate largely depends on the momentum transfer of the impinging jet.

Gardon and Akfirat [4] investigated the variation in local heat transfer rate with changes in the free stream turbulence at the nozzle exit. Hoogendoorn [5] studied the effect of turbulence on the stagnation heat transfer rate of impinging jets issuing from a long straight pipe. Zumbrunnen and Aziz [6] investigated the effect of flow intermittency on convective heat transfer to a planar water jet impinging on a constant heat flux surface. Al-Salam et al. [7] found that the heat transfer coefficient has a linear relationship with the standard deviation of the freestream velocity in stagnation flow.

Mesh screens have been used to reduce free stream turbulence and non-uniformity of mean velocity by suppressing swirls and velocity fluctuations. Baines and Peterson [8] found that a downstream distance of 5–10 mesh lengths was required to ensure reasonably good flow establishment. Laws and Livesey [9] investigated

* Corresponding author. Tel.: +82-54-279-2169; fax: +82-54-279-3199.
E-mail address: sjlee@postech.ac.kr (S.-J. Lee).

0017-9310/$ - see front matter © 2004 Elsevier Ltd. All rights reserved.
doi:10.1016/j.ijheatmasstransfer.2003.12.002

Nomenclature

A	area of gold-coated film (heating area)	T_a	ambient temperature
d	internal diameter of nozzle	T_j	jet exit temperature
f	non-uniformity factor of gold-coated film	T_w	local wall temperature
h	local heat transfer coefficient, Eq. (1)	U	mean velocity
I	electric current across the gold-coated film	u'	local RMS velocity fluctuation, $\sqrt{\overline{u'^2}}/U_e$
k	thermal conductivity of air	U_c	mean streamwise velocity along the jet centerline
Nu	local Nusselt number, Eq. (1)		
$\overline{Nu}$	average Nusselt number, Eq. (2)	U_e	jet exit velocity
q_c	conduction heat flux	V	voltage across the gold-coated film
q_v	convection heat flux	z	distance between the nozzle exit and the impingement plate
r	radial distance from the stagnation point		
Re	jet Reynolds number, $U_e d/v$	σ_s	solidity ratio of the mesh screen

the effect of gauze screens on the downstream flow structure, including the mean velocity and turbulence intensity. Tan-Atichat and Nagib [10] reported that the performance of screens and perforated plates depended on the incoming flow characteristics such as the mean velocity, turbulence level and power spectral density. Groth and Johansson [11] studied the turbulence suppression effect of screens over a wide range of mesh sizes. They found that in the region just behind a single screen, the turbulent structure is highly anisotropic and the turbulence intensity is higher than that of the upstream flow. The turbulence intensity decreases rapidly in the initial region of 15–25 mesh lengths. Thereafter, it falls below the turbulence level of the incoming flow. However, the use of mesh screens to enhance the heat transfer rate of an impinging jet has received little attention.

The objective of present study was to investigate the effects of free stream turbulence on the heat transfer rate of an impinging round jet for various mesh screens. To better understand the heat transfer characteristics on the impingement plate, the mean velocity and turbulence intensity profiles of the impinging jet issuing from a sharp-edged orifice nozzle were measured using hot-wire anemometry and the near-field flow field was visualized using a smoke-wire technique.

2. Experimental apparatus and method

2.1. Experimental apparatus

A schematic diagram of the experimental apparatus is shown in Fig. 1. In the experimental system, compressed air is passed through a heat exchanger, an orifice flowmeter, a flexible tube, a honeycomb, a long straight PVC pipe and a mesh screen before entering a sharp-edged orifice nozzle. A heat exchanger was installed to adjust the air temperature such that the jet temperature was within ±0.1 °C of the ambient room temperature. The flow rate was measured with an ASME standard orifice flowmeter with ±1% reading accuracy. A circular straight PVC pipe with an internal diameter of 52.3 mm and a length of 2.5 m was used. The pipe was rigidly mounted on a traverse with which the nozzle-to-plate spacing could be adjusted with a resolution of 0.01 mm. Throughout all the experiments, the pressure drop was within ±1.5%.

A sharp-edged orifice nozzle was attached at the downstream end of the long pipe as shown in Fig. 2. The inside diameter and thickness of the orifice nozzle were 25 and 5 mm, respectively. A screen holder with an inside diameter the same as that of the PVC pipe was installed 35 mm upstream of the jet nozzle to hold the mesh screen. One thermocouple was installed at 20 mm upstream of the nozzle exit to measure the jet temperature. Another thermocouple was placed near the impingement region to monitor the ambient air temperature.

The heated impingement plate was composed of a plexiglas flat plate, a transparent gold-coated film and thermocouples as shown in Fig. 2. The dimensions of the plexiglas plate, which had low thermal conductivity, were 303×303 mm^2 with a thickness of 12.7 mm. The transparent vacuum-deposited gold-coated film, which had dimensions of 120 mm (length) × 40 mm (width) × 127 μm (thickness), was glued to the plexiglas plate. Two copper-foil strip electrodes, each of thickness 100 μm, were attached to the end sides of the film, and then silver paint was applied to establish a good electrical contact between the electrode and the upper surface of the film. The electrodes were connected to a DC power supply (HP6555A) in series with a shunt register rated 50 mV and 5 A, allowing adjustable DC voltage to the electrodes. When a DC electric current was applied to the heated plate, an almost uniform wall heat flux boundary condition was ohmically established on the gold-coated film.

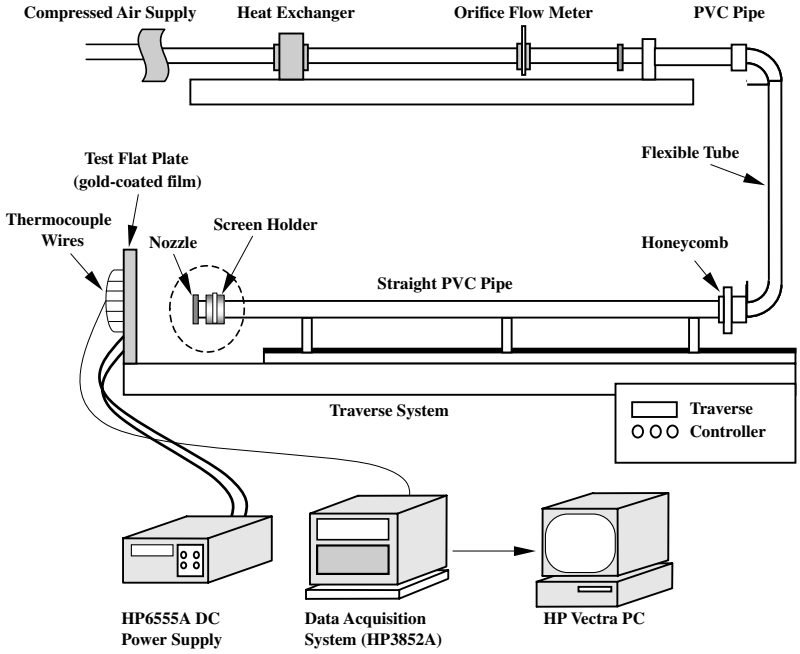

Fig. 1. Schematic diagram of experimental set-up.

The HP3852A data acquisition system was used to measure the electric voltage drop (V) across the film and the current input (I) to the shunt register. Thirty-three T-type thermocouples of diameter 200 μm were installed through circular holes of the plexiglas plate to contact with the film. The thermocouples were connected to the HP3852A data acquisition system. The temperature measurement accuracy for this system was about 0.08 °C. To minimize heat conduction through the impinging plate, two styrofoam plates of each thickness 10 mm were placed on the backside surface of the plexiglas.

Fig. 3 shows the experimental set-up used for the smoke-wire flow visualization. A fine nichrome wire (diameter 100 μm) was placed horizontally about 1 mm downstream of the nozzle exit. When electric power was applied to the smoke-wire coated with SAFEX fog fluid, small droplets of SAFEX fluid evaporated to produce white smoke filaments. A thin laser light sheet produced by passing a pulsed Nd-YAG laser through a cylindrical lens illuminated the smoke streamlines, revealing the flow pattern. Shortly before the laser firing, the shutter of the digital camera (Olympus C-3030) was opened. To obtain clear flow images with good contrast, the pulsed laser, digital camera and a DC power supply were synchronized using a four-channel delay generator.

A single hot-wire probe (Dantec 55P11) was used to measure the streamwise mean velocity and turbulence intensity of the impinging jet. This hot-wire probe was connected to a constant temperature anemometer (TSI IFA-100). The velocity signal from the hot-wire anemometer was digitized with an A/D converter (DT2838) after 800 Hz low-pass filtering.

2.2. Data reduction and uncertainty analysis

The local convective heat transfer rate and corresponding Nusselt number at a particular position are calculated using the following equations:

$$h = \frac{q_v}{(T_w - T_j)}, \quad Nu = \frac{hd}{k}, \tag{1}$$

where q_v is the convective heat flux, k and T_j are the thermal conductivity of air and jet exit temperature, respectively. Typical values for the temperature difference ($T_w - T_j$) are in the range of 8–20 K for a uniform heat flux of 1000 Wm^{-2} on the impingement plate. Each temperature was obtained by averaging 60 readings. The convective heat flux q_v was obtained by subtracting the energy losses (q_c) from the total heat flux imposed on the film. The radial heat conduction was calculated by solving the one-dimensional energy equation along the radial direction of the plate. The lateral heat conduction was negligible due to the styrofoam insulation. More detailed data reduction procedures are described in [1]. The maximum conduction heat flux, q_c, was estimated as about 3% of the total imposed heat flux.

The local heat transfer rates were averaged to obtain an average Nusselt number, which is defined as

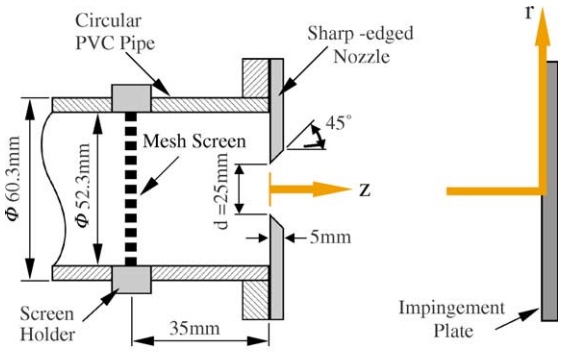

	ScreenA	ScreenB	ScreenC	ScreenD	ScreenE
σ_s	0.00	0.25	0.60	0.71	0.83

(a)

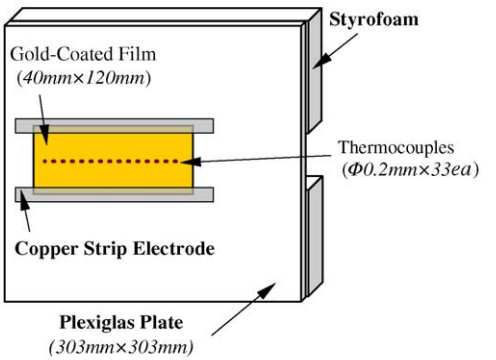

(b)

Fig. 2. Schematic diagram of (a) jet nozzle and (b) impingment plate.

$$\overline{Nu} = \frac{q_v d}{k(\overline{T_w} - \overline{T_j})} = \left[\frac{2}{r^2}\int_0^r \frac{r\,dr}{Nu(r)}\right]^{-1}. \quad (2)$$

The integral was solved using the Newton–Cotes formula with three-point correlation based on measured local Nusselt numbers.

The uncertainty in the local Nusselt number determination was estimated using the method suggested by Kline and McClintock [12] with a 95% confidence level. The total uncertainty estimated for the local Nusselt number ranged from 2.84% to 3.72%. The individual contributions to the total uncertainty are listed in Table 1. The primary contributor to the uncertainty is the factor f which accounts for non-uniformity of the gold-coated film. For the heat flux calculation, a value of $f \approx 1$ was adopted in this study. Another significant source of uncertainty is the wall temperature T_w. The conduction heat flux q_c and the electric input voltage V are the next two most significant contributors to the uncertainty. The uncertainties in the Reynolds number calculation and radial position (r/d) along the plate are estimated to be within 2.46% and 0.70%, respectively. The measurement uncertainties estimated for the mean velocity and turbulence intensity are less than 1.35% and 3.45%, respectively.

3. Results and discussion

3.1. Flow visualization

The impinging jet on a flat plate was visualized for five mesh solidities of $\sigma_s = 0.00$, 0.25, 0.60, 0.71 and 0.83. Fig. 4 shows typical flow images of the impinging jet at the conditions of $Re = 15,000$ and $z/d = 2$. The smoke streaks clearly show that the vortex filaments and the evolution of vortex formation are symmetric about the flow axis. The toroidal vortices, which result from an intrinsic unstability in the outer shear layer of the impinging jet, impinge on the heated flat plate at the lateral edge of the pipe nozzle (i.e., $r/d = 0.5$). The convecting wall eddies induced by the interaction between the large-scale toroidal vortices and the impingement surface are seen in the region $0.9 \leqslant r/d \leqslant 1.6$. These eddies seem to be responsible for the additional enhancement of the local heat transfer rate in that region.

The flow structure in the central region of the jet flow is almost the same for all mesh solidities, because the impingement plate is placed within the potential core. In contrast, the outer shear layer of the jet easily loses momentum and becomes highly turbulent. The flow patterns in Fig. 4 reveal that the axial distance beyond which the impinging jet becomes unstable is closely related to the mesh solidity. The larger the mesh solidity, the shorter the critical distance becomes. For mesh screens of larger solidity, the entrainment of ambient fluid into the jet is enhanced, changing the jet flow characteristics [13]. Additionally, increase of the mesh solidity leads to increases in the vortex spacing between consecutive vortices in the downstream direction and the size of the toroidal vortices.

3.2. Flow structure

To understand the flow structure of the impinging jet, the streamwise mean velocity (U) and turbulence intensity of the streamwise velocity component of the free jet (i.e., the component along the Z axis) were measured. Since the impingement plate was removed for the hot-wire measurements, the nozzle-to-plate spacing indicates the distance between the nozzle exit and the tip of hot-wire probe.

The mean velocity distributions at six downstream locations for five mesh solidities are compared in Fig. 5. At the downstream location of $z/d = 0.2$, the mean velocity is approximately constant in the central region

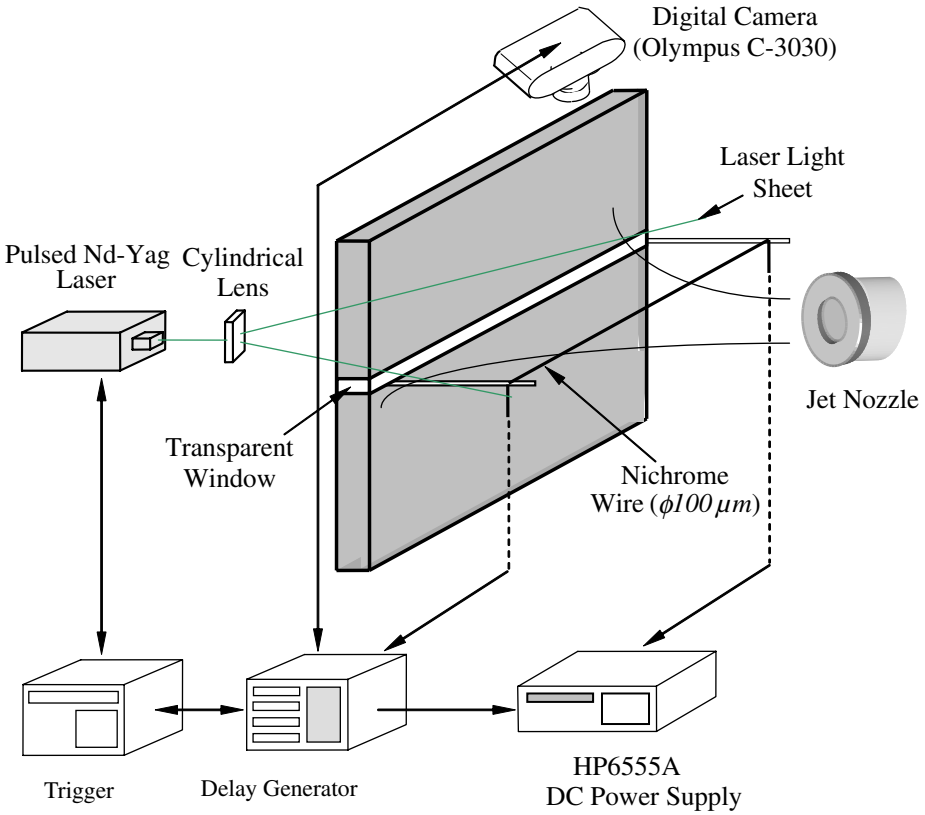

Fig. 3. Experimental set-up for smoke-wire flow visualization.

Table 1
Uncertainty analysis for local Nusselt numbers

Individual measured value		$\left\lvert\frac{\delta x_i}{Nu}\frac{\partial Nu}{\partial x_i}\right\rvert \times 100(\%)$
x_i	Unit	
f	–	2.08–2.52
T_w	°C	1.43–2.32
V	V	0.65–1.12
I	A	0.44–1.20
q_c	W/m^2	0.18–2.11
T_a	°C	0.01–0.15
T_j	°C	0.01–0.13
A	m^2	0.08
k	W/m K	0.06
Total uncertainty: $\frac{\delta Nu}{Nu} = 2.84$–$3.72$ (%)		

of the jet, irrespectively of the mesh solidity. The mean velocity decreases rapidly at $r/d = 0.45$–0.5. On moving downstream, however, the central region of constant mean velocity is gradually reduced and disappears at $z/d = 4.0$. Thereafter, the mean velocity has a bell-shaped distribution. With going downstream, the maximum velocity at the jet center decreases and the jet width expands. The effect of increasing mesh solidity manifests as an increase in the shear layer velocity gradient. As the flow goes downstream, the difference in axial mean velocity is reduced for various mesh solidity. At $z/d = 10.0$, the mean velocity distribution is almost identical for the five mesh solidities. This can be primarily attributed to the self-preserving flow characteristics of the turbulent jet due to loss of jet momentum and active mixing with entrained ambient fluid.

The radial profiles of the axial turbulence intensity corresponding to the mean velocity rofiles of Fig. 5 are depicted in Fig. 6. For $z/d = 0.2$, the turbulence intensity has a sharp peak at approximately $r/d = 0.47$. However, irrespective of the mesh solidity, the turbulence intensity is small (less than 1%) at the center of the jet. As the jet develops with going downstream, the turbulence intensity increases in the impingement region. This increase in turbulence intensity continues up to the downstream location of $z/d = 6$, indicating that the jet flow has been, somewhat, fully developed. On going further downstream, the turbulence intensity decreases gradually. The turbulence intensity has its maximum value at the location of $z/d = 2$ and $r/d = 0.45$. The radial location of maximum turbulence intensity moves slightly toward the jet center with going

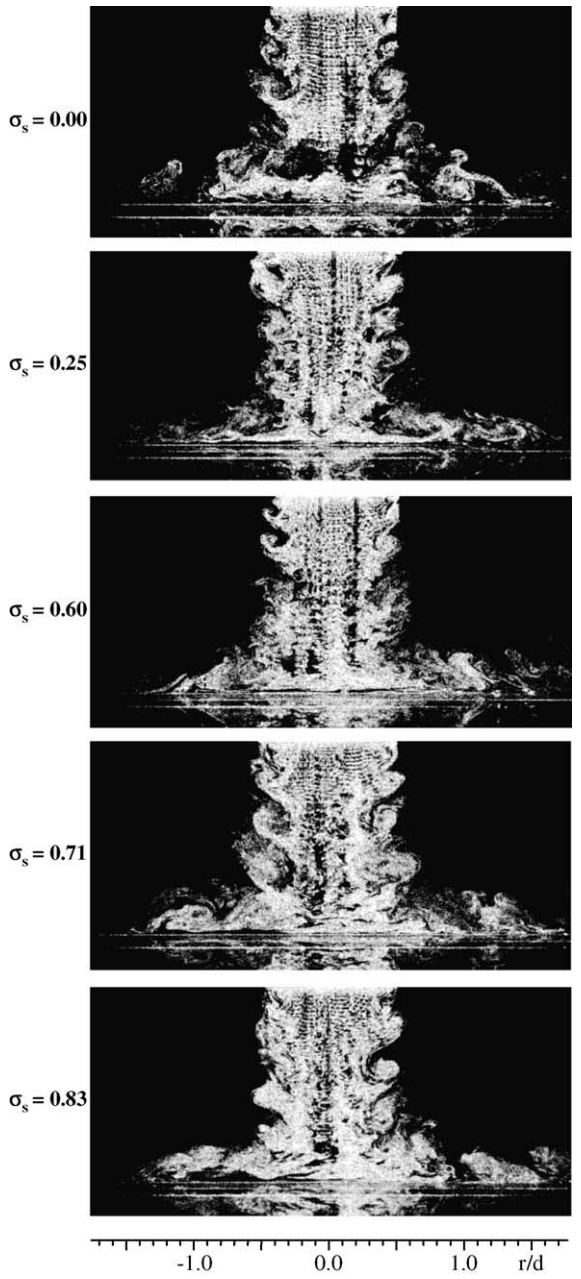

Fig. 4. Typical flow visualization images of impinging jet for systems with various mesh solidities at $Re = 15,000$ and $z/d = 2$.

downstream, possibly as a result of the vena contracta effect of sharp-edged orifice jets. Further downstream, the sharp peak in the turbulence intensity distribution becomes blunt due to active mixing and turbulent diffusion. At $z/d = 10$, the streamwise turbulence intensity at the jet center is similar for the five different mesh solidities.

The general shape of all the turbulence intensity profiles looks similar, irrespective of mesh screen. At a moderate nozzle-to-plate spacing, however, the effect of mesh solidity on the turbulence intensity distribution is evident (see Fig. 6). In the central region ($r/d < 0.5$) of the free jet, the axial turbulence intensity is increased with increasing the mesh solidity. However, a different trend is observed in the outer region. At the downstream distances of $z/d = 4.0$ and 6.0, the turbulence intensity is larger for all cases with mesh screens than that without a screen. This indicates that the mesh screens cause more vigorous velocity fluctuations in the near field.

The mean velocity and turbulence intensity profiles measured along the jet centerline for various mesh solidities are shown in Fig. 7. In this figure, all the data were non-dimensioned by the jet exit velocity U_e. Beyond the potential core length of $z/d = 4$, the normalized velocity decreases gradually. At the downstream distance of $z/d = 10$, the centerline velocity is reduced to half of the jet exit velocity. For all mesh solidities, the centerline velocity is similar in the near field ($z/d \leqslant 2$). Further downstream, however, the centerline velocity becomes dependent on the mesh solidity: as the mesh solidity increases, the centerline velocity decreases.

The variation in turbulence intensity along the jet centerline is shown in Fig. 7(b). In this figure, the results of Baines and Perterson [8] for $\sigma_s = 0.438$ and $Re = 12,500$ are included for comparison. The turbulence intensities increase rapidly with increasing z/d up to $z/d = 6$, where they have maximum values, and then decrease monotonically on going further downstream. The present results show a similar trend to those of Baines and Peterson [8], although the magnitudes and peak locations are noticeably different. These discrepancies may be mainly attributed to differences in nozzle configuration with the difference in Reynolds number. Their results show a peak value at $z/d = 8$. In the present study with a sharp-edged orifice nozzle, however, the peak occurs at the location of $z/d = 6$. With increasing mesh solidity, the turbulence intensity increases at moderate nozzle-to-plate spacings less than $z/d = 7$. Further downstream, the turbulence intensity decreases faster as the flow moves downstream for systems with mesh screens than that for the no screen case.

3.3. Heat transfer characteristics

The effect of mesh solidity on local heat transfer rate is illustrated in Fig. 8 for the nozzle-to-plate spacings of $z/d = 0.2$–10. For all mesh solidities, the general shape of the local Nusselt number distribution is similar at a given nozzle-to-plate spacing, although the magnitude varies slightly with the change of mesh solidity. The local heat transfer rate increases initially with radial distance from the stagnation point and exhibits a peak at around $r/d = 0.4$. Thereafter, it decreases rapidly.

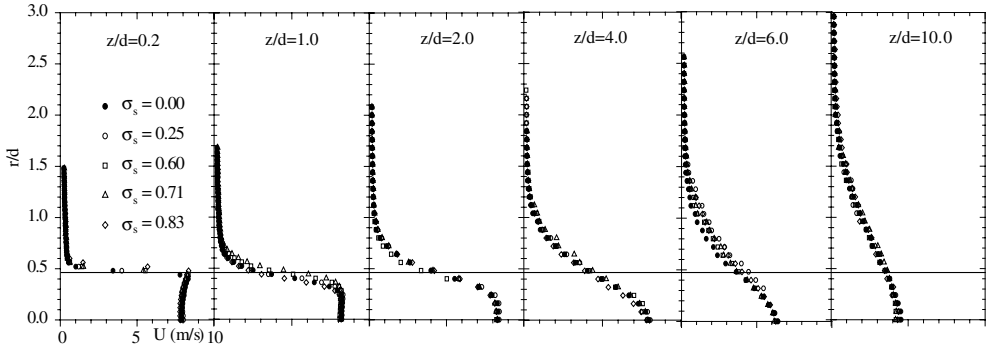

Fig. 5. Streamwise mean velocity profiles for five mesh solidities.

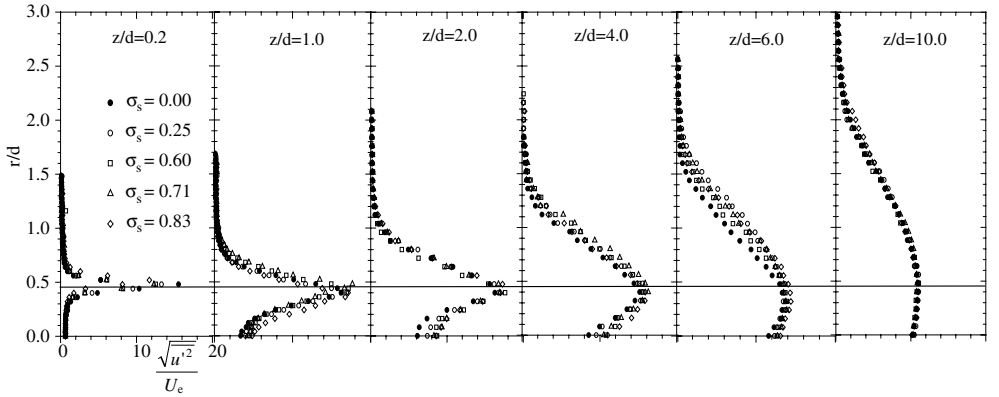

Fig. 6. Variation of turbulence intensity profile with respective to mesh solidity.

The local heat transfer rates in the radial direction increase with mesh solidity and nozzle-to-plate spacing tested in this study except for the case of $z/d = 0.2$. This increase seems to be caused by a noticeable elevation in the turbulence intensity of the impinging jet due to the presence of the mesh screen in the approaching stream and jet diffusion with going downstream. The initial enhancement of the local heat transfer rate at $z/d = 0.2$ results from the higher impingement velocity at this downstream distance. Lytle and Webb [14] also observed significantly higher radial velocities near the nozzle exit (at $z/d = 0.1$), reaching magnitudes more than double the jet exit velocity.

The local Nusselt number distributions show moderate variation in the radial location of $0.9 \leqslant r/d \leqslant 1.6$. This is in accordance with the location of convecting wall eddies over the impingement surface shown in Fig. 4. For smaller nozzle-to-plate spacings ($z/d \leqslant 4$), the local Nusselt number distribution has a second peak at around $r/d = 1.53$. On going further downstream ($z/d > 4$), this second peak disappears and the local Nusselt number decreases monotonically beyond the first peak. In this downstream region, the convective heat transfer rate decreases with increasing mesh solidity and nozzle-to-plate spacing. Pan et al. [15] reported similar results for a turbulent liquid jet.

For comparison purposes, Fig. 8 also shows the results of Gardon and Akfirat [4] recorded at $z/d = 2$ for a contoured nozzle. The contoured jet shows two peaks at radial locations similar to those observed in the present work, although overall the *Nu* magnitude is much less than that in the present results. In fact, irrespective of mesh screen solidity, the heat transfer rate in the impingement region for a sharp-edged orifice jet is about 25% greater than that obtained previously using a contoured nozzle jet. This heat transfer enhancement can be primarily attributed to the larger velocity gradient and higher turbulence intensity of sharp-edged orifice jets. With increasing mesh solidity, the heat transfer enhancement increases from 24% to 27%.

The local Nusselt number values at the stagnation point, the first peak, and the second peak vary with changes in the nozzle-to-plate spacing and mesh solidity. For all nozzle-to-plate spacings, the local heat transfer

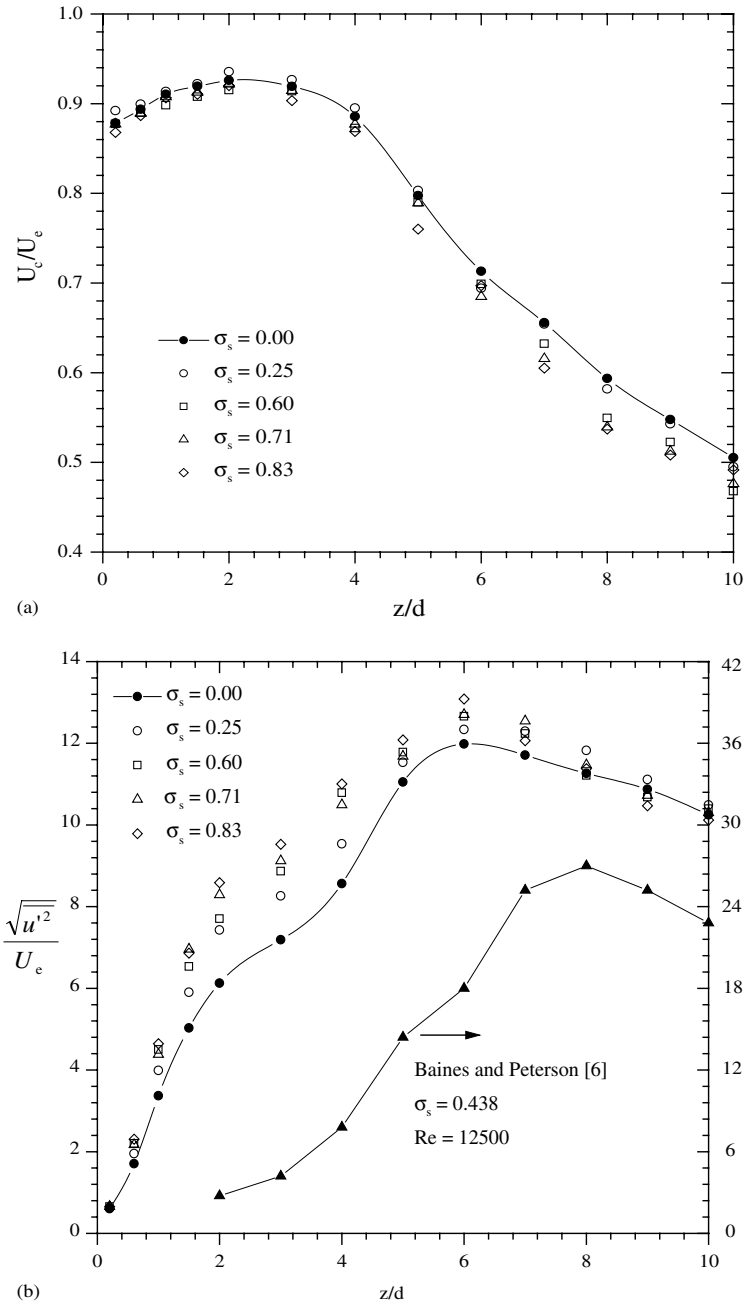

Fig. 7. (a) Mean velocity and (b) turbulence intensity distributions along the jet centerline.

rate at the first peak is approximately 4–8% higher than that at the stagnation point. This coincides with the previous results of Pan et al. [15] and Lee and Lee [2]. The magnitude and presence of the secondary peak are largely dependent upon the nozzle-to-plate spacing. Contrary to the case of the first peak, the ratio of the local heat transfer rate at the second peak to the stagnation point value tends to decrease with increasing axial distance from the nozzle exit.

The pressure gradient usually serves to stabilize the laminar boundary layer in the impingement region, despite the high turbulence levels in the free jet stream. Zhou et al. [16] examined the pressure gradient distribution along the impingement plate and confirmed that

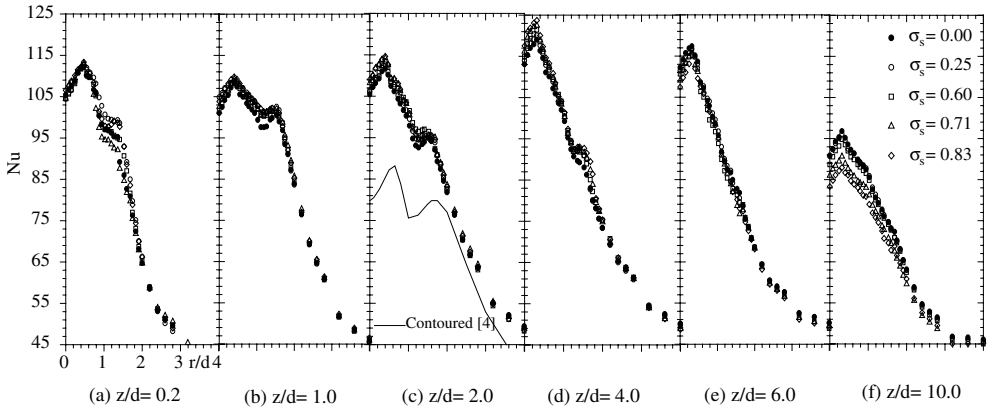

Fig. 8. Variation of local Nusselt number with respective to nozzle-to-plate spacing for various mesh solidities.

the transition from laminar to turbulent boundary layer flow was triggered by the disappearance of the pressure gradient in the spreading wall jet. The locations of the second peak in local heat transfer rate distribution coincide with that of induced toroidal vortices shown in Fig. 4, indicating transport of high turbulent energy there. The ring-shaped toroidal vortices formed on the impingement surface generate a separating boundary between the stagnation region and the wall jet, increasing the local heat transfer coefficients at the secondary peak location.

The presence of a mesh screen with larger solidity seems to reduce the discrepancy of the pressure gradient along the impingement plate, leading to a flattening of the heat transfer distribution around the second peak for large mesh solidities. Compared with the contoured nozzle results of Gardon and Akfirat [4], the second peak obtained using the sharp-edged orifice nozzle is located slightly upstream due to faster velocity decay in the radial direction. At downstream locations of $z/d = 4$, the second peak is not observed and the effect of the mesh screen on the heat transfer enhancement is the opposite of that observed at $z/d < 4$.

The variation of the local Nusselt number at the first peak with respect to the nozzle-to-plate spacing is shown in Fig. 9. For five mesh solidities tested in this study, as the nozzle-to-plate spacing increases, the magnitude of the first peak decreases initially up to a minimum at $z/d = 0.6$, and then rapidly increases up to a maximum value at $z/d = 4$. Beyond this peak, the heat transfer rate decreases monotonically. This trend is the same as that observed for the stagnation heat transfer rate, with the exception of the downstream distance of $z/d = 0.2$.

The mesh screen does not alter the location of maximum heat transfer rate. However, the effect of mesh solidity on local heat transfer is enhanced with increasing the nozzle-to-plate spacing up to the end of the potential core ($z/d \approx 4$). At $z/d = 4$, the maximum heat transfer rate for the system with a mesh solidity of $\sigma_s = 0.83$ is about 3.92% larger than that without a screen. It is worth noting that at $z/d = 5$ the values of the Nusselt number at the first peak have converged to a single value that is independent of the mesh solidity. However, on further increase of the nozzle-to-plate spacing beyond $z/d = 5$, the peak value decreases rapidly with increasing mesh solidity. Thus, the effect of the mesh screen on the heat transfer enhancement is most effective at $z/d = 4$, around the potential core length, or at a slightly smaller axial distance.

In the local Nusselt number distributions, the first peak usually occurs in the vicinity of the nozzle edge, regardless of whether the flow is laminar or turbulent. Zhou et al. [16] found that the maximum pressure gradient occurs at approximately a radial location of $r/d = 0.5$. This location seems to be closely related to the inherent flow structure of the impinging submerged air jets. The large pressure gradient accelerates the fluid movement outward along the impingement plate, resulting in a thin thermal boundary layer. It therein seems to contribute to higher heat transfer rate. On the other hand, as shown in Figs. 4 and 5, the large-scale toroidal vortices strike at the location of the first peak in the heat transfer rate on the impingement plate, where the turbulence intensity has a maximum value. The combined effect of above two factors seems to lead to the formation of the first peak in the local Nusselt number distribution. Since these two factors are only related to the nozzle exit configuration, the radial location of the first peak remains almost independent of the mesh solidity and nozzle-to-plate spacing.

Fig. 10 shows the variation of the average Nusselt number with respect to mesh solidity (σ_s). Irrespective of mesh solidity, the average Nusselt number increases noticeably with increasing nozzle-to-plate spacing up to a downstream location of $z/d = 2$, after which it monotonically decreases. When the nozzle-to-plate

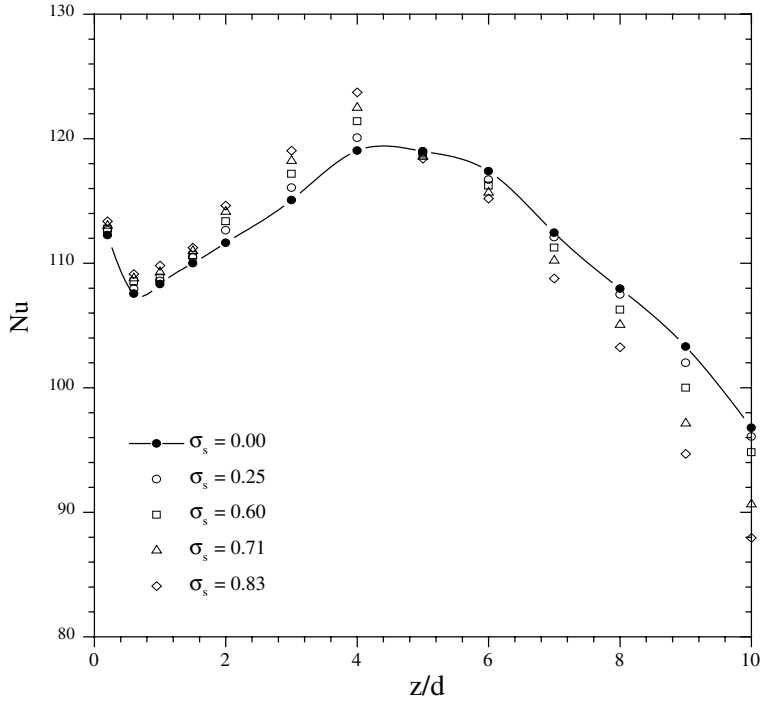

Fig. 9. Variation of local maximum Nusselt number as a function of nozzle-to-plate spacing (z/d) and mesh solidity (σ_s).

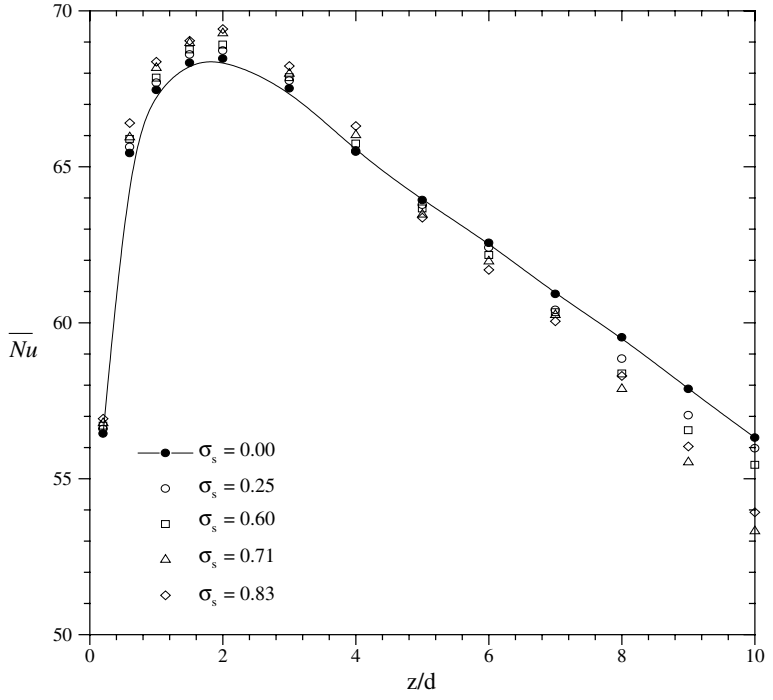

Fig. 10. Average Nusselt number as a function of mesh solidity.

spacing is smaller than the potential core, the average Nusselt number increases with increasing mesh solidity. This results from the increase of the turbulence level of the impinging jet at larger values of the mesh solidity. Compared to the system without a screen, the augmentation ratios of the average Nusselt numbers at $z/d = 2$ for the systems with screens of $\sigma_s = 0.25$, 0.60, 0.71 and 0.83 are 0.37%, 0.66%, 1.19% and 1.38%, respectively. The increase in turbulence intensity caused by increasing the mesh solidity is accompanied by a decrease in the jet momentum in the near field and a reduction in the potential core length. This lower jet momentum has mostly decayed at downstream locations beyond $z/d = 4$.

Consequently, the average Nusselt numbers decrease with increasing mesh solidity and nozzle-to-plate spacing. The inclusion into the system of the screen of $\sigma_s = 0.71$ reduces the average heat transfer rate at $z/d = 10$ by about 5.62%. Thus, it can be concluded that the mesh screen effectively enhances heat transfer only when the nozzle-to-plate spacing is smaller than the potential core. For $z/d > 4$, on the contrary, the installation of a mesh screen leads to a decrease in the heat transfer rate.

4. Conclusions

The effect of installing a mesh screen upstream of the jet nozzle on the impinging jet heat transfer was investigated experimentally at a fixed jet Reynolds number of $Re = 15,000$ with varying the mesh solidity σ_s and the nozzle-to-plate spacing z/d. Visualized flows of the impinging jets clearly revealed the vortex structures on the impingement plate. The location of the vortex eddy coincided exactly with the peak in the local Nusselt number distribution. Flow structure measurements using a hot-wire anemometry showed that the turbulence intensity increases with increasing mesh solidity (σ_s) and has a maximum value at the radial location $r/d = 0.47$. The local heat transfer rate was highest at around $r/d = 0.4$. The local Nusselt numbers at the first peak were about 4–8% larger than that at the stagnation point, irrespective of the nozzle-to-plate spacing and mesh solidity.

The presence of the mesh screen moderately enhanced the heat transfer rate in the impingement region for nozzle-to-plate spacings of $z/d \leqslant 4$. This enhancement is attributed to the fact that the mesh screens modify the flow structure such that the turbulence intensity of the impinging jet is increased within the potential core. The local and average heat transfer rates increased with mesh solidity and nozzle-to-plate spacing, displaying local maximum values at $z/d = 4.0$ and 2.0, respectively. Among the five mesh screens tested in this study, the screen of solidity $\sigma_s = 0.83$ increased the local maximum heat transfer rate about 3.92% at $z/d = 4.0$ and the average Nusselt number was enhanced about 1.38% at $z/d = 2.0$, compared with those for the case of no screen. However, as the mesh screen increases the turbulence intensity at the expense of jet momentum, the heat transfer rate is reduced at further downstream locations ($z/d > 4.0$).

Acknowledgements

This work was supported by a NRL (National Research Laboratory) project sponsored by the Ministry of Science and Technology (MOST) of Korea.

References

[1] J.H. Lee, S.J. Lee, The effect of nozzle aspect ratio on stagnation region heat transfer characteristics of elliptic impinging jet, Int. J. Heat Mass Transfer 43 (3) (2000) 555–575.
[2] J.H. Lee, S.J. Lee, The effect of nozzle configuration on stagnation region heat transfer enhancement of axisymmetric jet impingement, Int. J. Heat Mass Transfer 43 (23) (2000) 3497–3509.
[3] Z.Y. Guo, D.Y. Li, B.X. Wang, A novel concept for convective heat transfer enhancement, Int. J. Heat Mass Transfer 41 (16) (1998) 2221–2225.
[4] R. Gardon, J.C. Akfirat, The role of turbulence in determining the heat transfer characteristics of impinging jets, Int. J. Heat Mass Transfer 8 (5) (1965) 1261–1272.
[5] C.J. Hoogendoorn, The effects of turbulence on heat transfer at a stagnation point, Int. J. Heat Mass Transfer 20 (6) (1977) 1333–1338.
[6] D.A. Zumbrunnen, M. Aziz, Convective heat transfer enhancement due to intermittency in an impinging jet, J. Heat Transfer 115 (1993) 91–98.
[7] H. Al-Salam et al., Effect of turbulence on heat transfer in stagnation flow, J. Thermophys. Heat Transfer 10 (2) (1996) 290–296.
[8] W.D. Baines, E.G. Peterson, An investigation of flow through screens, J. Fluid Mech. 73 (2) (1951) 467–480.
[9] E.M. Laws, J.L. Livesey, Flow through screens, Ann. Rev. Fluid Mech. 10 (2) (1978) 247–266.
[10] J. Tan-Atichat, H.M. Nagib, Interaction of free-stream turbulence with screens and grids: a balance between turbulence scales, J. Fluid Mech. 114 (3) (1982) 501–528.
[11] J. Groth, A.V. Johansson, Turbulence reduction by screens, J. Fluid Mech. 197 (1) (1988) 139–155.
[12] S.J. Kline, F.A. McClintock, Describing uncertainties in single-sample experiments, Mech. Eng. 75 (1) (1953) 3–8.
[13] C.O. Popiel, O. Trass, Visualization of a free an impinging round jet, Exp. Thermal Fluid Sci. 4 (2) (1991) 253–264.
[14] D. Lytle, B.W. Webb, Air jet impingement heat transfer at low nozzle-to-plate spacing, Int. J. Heat Mass Transfer 37 (7) (1994) 1687–1697.

[15] Y. Pan, J. Stevens, B.W. Webb, Effect of nozzle configuration on transport in the stagnation zone of axisymmetric impinging free surface liquid jets: Part II. Local heat transfer, J. Heat Transfer 114 (3) (1992) 880–886.

[16] D.W. Zhou, C.F. Ma, M. Qin, Effect of pressure gradient on heat transfer of impinging submerged circular jets, J. Thermal Sci. 11 (2) (2002) 180–185.